

A Euryhaline-Fish-Inspired Salinity Self-Adaptive Nanofluidic Diode Leads to High-Performance Blue Energy Harvesters

Junran Hao, Bin Bao, Jiajia Zhou, Yanshuai Cui, Xiachao Chen, Jiale Zhou, Yahong Zhou,* and Lei Jiang

The adaptability to wide salinities remains a big challenge for artificial nanofluidic systems, which plays a vital role in water–energy nexus science. Here, inspired by euryhaline fish, sandwich-structured nanochannel systems are constructed to realize salinity self-adaptive nanofluidic diodes, which lead to high-performance salinity-gradient power generators with low internal resistance. Adaptive to changing salinity, the pore morphology of one side of the nanochannel system switches from a 1D straight nanochannel (45 nm) to 3D network pores (1.9 nm pore size and $\approx 10^{13}$ pore density), along with three orders of magnitude change for charge density. Thus, the abundant surface charges and narrow pores render the membrane-based osmotic power generator with power density up to 26.22 W m^{-2} . The salinity-adaptive membrane solves the surface charge-shielding problem caused by abundant mobile ions in high salinity and increases the overlapping degree of the electric double layer. The dynamic adaption process of the membrane to the hypersaline environment endows it with good salt endurance and stability. New routes for designing nanofluidic devices functionally adaptable to different salinities and building power generators with excellent salt endurance are demonstrated.

kinds of ion channels embedded on the ionocyte membrane of the gills play a fundamental role in this process.^[4–6] In freshwater, ion absorptive channels (e.g., $\text{Cl}^-/\text{HCO}_3^-$ exchanger) are functioning, while in seawater, the counterparts responsible for salt secretion (e.g., $\text{Na}^+/\text{K}^+/\text{2Cl}^-$ cotransporter) will be activated and start to work (Figure 1A). Thus, the gills of salmon are able to transport ions from the external to the internal environments (absorption) or from the internal to the external environments (secretion). This vectorial ion transport is similar to the ion current rectification (ICR) behavior happening in ionic diodes. Thus, this ion channel system of euryhaline fish can be regarded as a biodiode whose rectification direction can be regulated by osmotic pressure in different salinities. As for artificial nanofluidic diodes, although rectification direction has been successfully modulated by electric field,

salinity-induced reversal of diode direction has never been realized and self-adaptive adjustment of nanochannel with changing salinity still remains a great challenge. Most of the reported artificial diodes show poor salt tolerance and only function in dilute solution.^[7–16] Ionic diodes highly depend on the ionic strength and fail in concentrated solution, for the surface charges on the inner wall of the channels tend to be


1. Introduction

Adapting to changing environments is an art displayed by creatures, like euryhaline fish, the leafy seadragon (*Phycodurus eques*), and the chameleon.^[1,2] The salmon, a typical euryhaline fish, survives both in river water and seawater by adaptively regulating ion transport with external environment change.^[3] Two

J. Hao, J. Zhou, Y. Zhou, L. Jiang
Key Laboratory of Bio-inspired Materials and Interfacial Science
Technical Institute of Physics and Chemistry
Chinese Academy of Sciences
Beijing 100190, P. R. China
E-mail: zhouyh@mail.ipc.ac.cn

B. Bao, Y. Zhou, L. Jiang
Beijing Advanced Innovation Center for Biomedical Engineering
Beihang University
Beijing 100191, P. R. China

J. Zhou
South China Advanced Institute for Soft Matter Science and Technology
School of Emergent Soft Matter
South China University of Technology
Guangzhou 510640, P. R. China

 The ORCID identification number(s) for the author(s) of this article can be found under <https://doi.org/10.1002/adma.202203109>.

Y. Cui
State Key Laboratory of Solid Waste Reuse for Building Materials
Beijing Building Materials Academy of Sciences Research
Beijing 100041, P. R. China

X. Chen
School of Materials Science and Engineering
Zhejiang Sci-Tech University
Hangzhou 310018, P. R. China

Y. Zhou, L. Jiang
School of Future Technology
University of Chinese Academy of Sciences
Beijing 100190, P. R. China

L. Jiang
Department of Chemical and Biological Engineering
Monash Centre for Membrane Innovation
Monash University
Clayton, Victoria 3168, Australia

DOI: 10.1002/adma.202203109

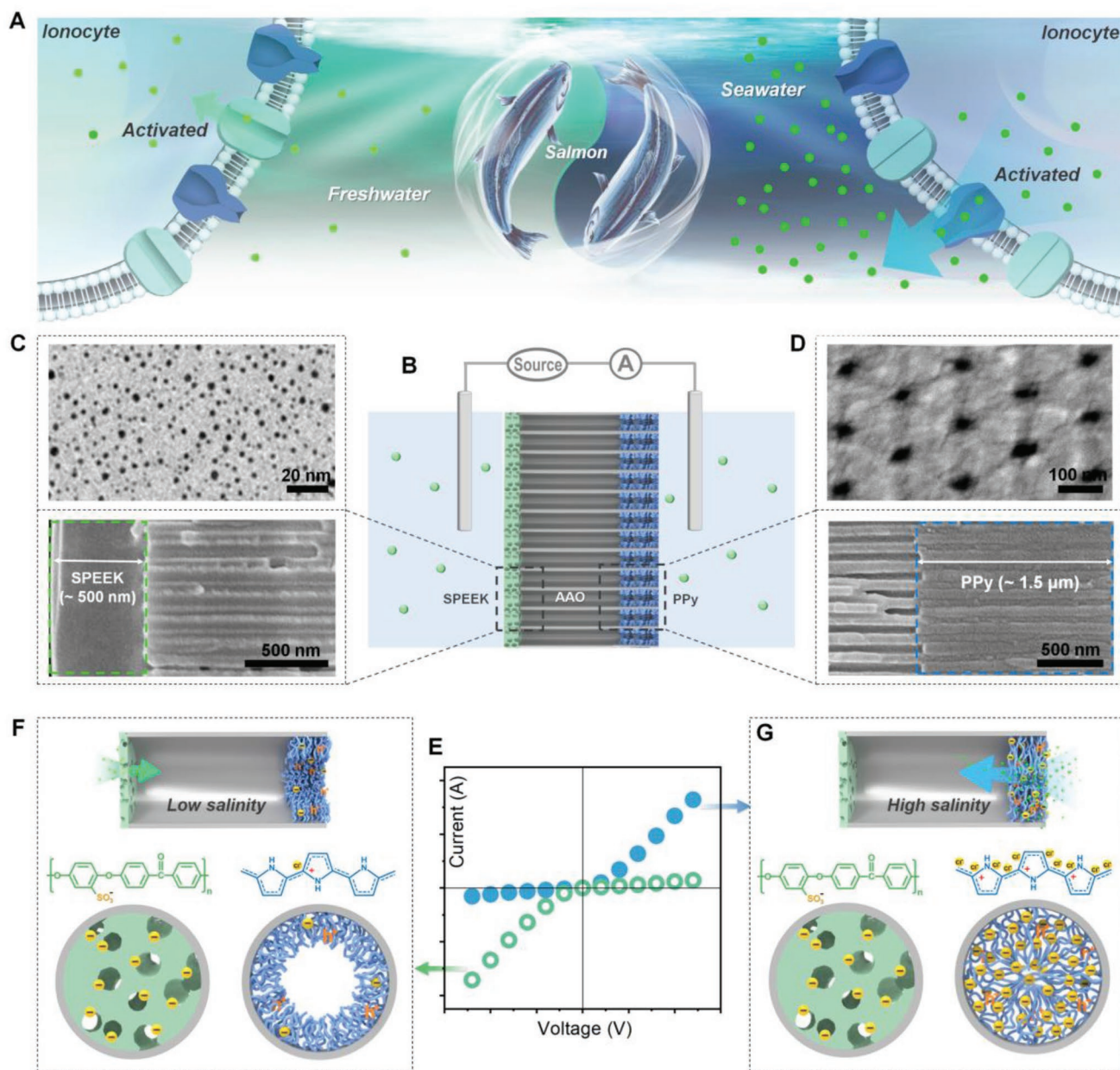


Figure 1. Schematic depiction of the salmon-inspired salinity self-adaptive nanofluidic diode with inversed rectification in a wide concentration range. A) Osmoregulation process by ion uptake (left) or ion release (right) through biological ion channels in a euryhaline fish. B) Schematic of the SPEEK/AAO/PPy sandwich-structured membrane-based ionic diode and the electrochemical device for testing the ion rectification properties. Characterization of the sandwich-structured nanochannels. C) Cross-section scanning electron microscopy (SEM) image and transmission electron microscopy (TEM) image of the SPEEK side with thickness of ≈ 500 nm and pore size of ≈ 2 nm. D) Cross-section and top-view SEM images of the polypyrrole side with tube length of ≈ 1.5 μm and pore diameter ≈ 45 nm. E) The direction-reversible ion rectification of the salinity self-adaptive nanofluidic diode. Schematic of the self-adaptive adjustment of the nanochannel to different salinities. F) In low salt solution, PPy is in collapsed state with a small number of positive charges and 1D straight nanochannel, and ionomer side with high charge density dominates the ion transport direction. G) In high salt solution, the straight pore switches into 3D network pores. PPy dominates the ion transport from the PPy side to ionomer side, which is just the opposite direction of dilute solution.

screened by the counterions in the electrolyte.^[12,15,17] This ionic concentration limitation restricts the application of artificial nanochannels in real environment (≈ 0.15 M in biological beings and more than 0.5 M in seawater).^[18,19] Very recently, several works demonstrated abundant surface charge and narrow pore size benefit the ICR with strong ionic strength and constructed

ion diodes that can function in high salinity. However, those reported membranes cannot adjust themselves adaptively to the changing environment, causing the same ion transport direction under all salinities.^[16,19–21]

Salinity adaptability could also benefit the osmotic power generating process, especially for the reverse electro dialysis

(RED) method. Because the effect of fixed surface charge could be shielded by high concentrations of mobile ions under high salinity, the performance of generator based on RED would markedly decrease which limits the application.^[22] Therefore, the salinity adaptive biode in Salmon inspires us to engineer a membrane whose charge and structure can be self-adjusted facing euryhaline environment. The capability of fluctuating surface charge with the environment renders the nanofluidic device ability to work from freshwater to seawater and even hypersaline environments, which could greatly expand the application scope. Modulating surface charge adaptively with changing salinity depends on the interaction between the membrane and electrolyte ions. Particularly, when confined to the nanometer or sub-nanometer space, the interplay between porous membrane and electrolyte may behave quite specially. For example, ion penetrating into graphene made adaptive graphene gel film.^[23,24] Local changes in polymer packing were observed by nanoscale variations in ion uptake in semiconducting polymer membranes.^[25,26] Recent research reveals that charge density of semiconducting polymer could be tuned by different doping methods, and the efficient ion exchange doping mechanism could achieve doping levels of up to almost one charge per monomer unit.^[27,28] In nanoconfined electrolyte environment, it may behave quite uniquely along the reversible doping or de-doping process.

Here, inspired by the salmon, a salinity self-adaptive nanofluidic diode with direction-inversed rectification was constructed by integrating two functional parts (ionomer and conducting polymer), which can be respectively activated in low and high salinity, to one nanochannel system, and the self-adaptability of conducting polymer side to euryhaline environment endows the system good salt endurance. In low salinity, polypyrrole (PPy) chains have low charge density and remain in collapse state. The topology of PPy side is formed by parallel 1D straight nanochannel (45 nm pore diameter) with low charge density. Under this condition, the ionomer side with high charge density dominates the ion transport, that is, potassium ions preferentially transport from the ionomer side to the PPy side (Figure 1F). In high salinity, the adaptive adjustment of PPy's charge and structure leads to the inverse of predominant direction of ion transport (Figure 1E). Enormous osmotic pressure triggers chloride ions to penetrate and retain in the PPy chain in nanoconfined environment. Thus, the doping levels of the PPy were improved significantly with the salinity. Surface charge density of PPy in hypersaline is three orders of magnitude higher than that in dilute solution, along with the charge polarity inverse. With salinity change, pore morphology undergoes extraordinary switch, due to the doping ions moving into/out polymer chain induced by osmotic pressure. Pore morphology of PPy side switches from 1D straight nanochannel (45 nm) to 3D network pores (1.9 nm pore size and $\approx 10^{13}$ pore density). Thus, in concentrated solution, PPy dominates the ion transport from the PPy side to ionomer side, which is just the opposite direction in dilute solution (Figure 1G). Furthermore, the dynamic adaption process of the membrane to hypersaline environment is demonstrated by the gradual increase of transmembrane ion current. Excellent salt endurance of the PPy-based membrane makes it a good osmotic power generator with an ultrahigh power density of 26.22 W m^{-2} . We provide

new routes for designing nanofluidic devices functionally adaptable to different salinities and building power generators with good salt endurance.

2. Results and Discussion

2.1. Fabrication and Morphology of the Sandwich-Structured Membrane

In this work, the sandwich-structured membrane was fabricated by integrating two functional composites (sulfonated poly(ether ether ketone) (SPEEK) and PPy) into different sides of anodic aluminum oxide (AAO) template (Figure 1B, Figures S1 and S3, Supporting Information). After spraying Pt nanoparticles on one side of the AAO membrane, conducting polymer chlorine-doped PPy was then grafted to the interwall of AAO pores through electrochemical-polymerization approach, with the pore size being $\approx 45 \text{ nm}$ and the PPy length being $\approx 1.5 \mu\text{m}$ (Figure 1D). Subsequently, negatively charged ionomer SPEEK was spin-coated on the other side of the membrane, with a thickness of $\approx 500 \text{ nm}$. (SPEEK was prepared through the sulfonation reaction between PEEK and sulfuric acid as shown in Figure S2, Supporting Information). The nanostructure of SPEEK can be characterized by TEM after being stained with heavy metal^[29] and the pore size of this side is $\approx 2 \text{ nm}$ (Figure 1C). Thus, a sandwich-structured membrane with asymmetric distribution of two functional ends is obtained.

2.2. Direction-Inversed ICR Behavior in a Wide Range of Ionic Concentration

A series of experiments were performed to explore ICR behavior of the membrane under a wide range of ionic concentrations. A representative rectifying current–voltage curve in dilute solution is observed in Figure 2A. In this case, potassium ions prefer to travel from SPEEK end to PPy end, attributed to the higher negative surface charges and smaller pore size of SPEEK side. The current is slightly rectified in 0.1 M KCl solution and the membrane behaves as Ohmic resistance (Figure 2B). Surprisingly, the ICR phenomena still exist in high salinity of 1 M KCl solution and the ICR direction is inversed, that is the cations are preferentially transported from PPy side to SPEEK side, which is totally opposite with low salinity (Figure 2C). Still, the rectified current exists even in 2.5 M KCl solution with an inversed direction. With 0.1 M as the critical concentration, the sandwich-structured ion diode shows opposite rectification direction at low ($1, 10 \times 10^{-3} \text{ M}$) and high salinity ($1, 2.5 \text{ M}$), with the rectification ratio $\approx 3\text{--}6$ (Figure 2D). A similar behavior is also observed when replacing KCl with NaCl as testing electrolyte as shown in Figure S4, Supporting Information. In addition, pH effect on the rectification was also investigated (Section 6, Supporting Information). Rectifying ion current under high salinity is a quite unique phenomenon and inversion of ion transport direction in diodes triggered by salinity has never been reported before. We speculate that this salt-induced direction-inversed ICR behavior in a wide salinity range may be attributed to the self-adaptive changes of PPy

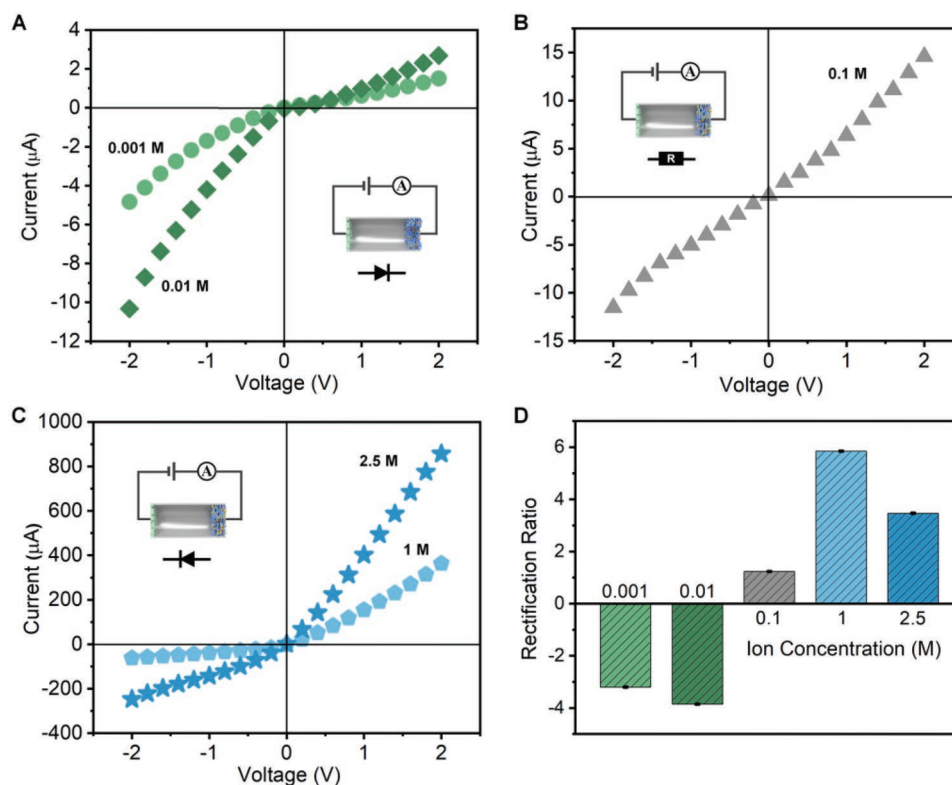


Figure 2. Salt-induced direction-inversed ion rectification behavior in a wide range of ionic concentration. A) In low ionic concentration of 1×10^{-3} M and 0.01 M, the sandwich-structured nanochannel behaves as the ion rectified current and preferentially conducts the current in one direction from the SPEEK side to the PPy side, that is the magnitudes of the currents at negative potentials are higher than those at positive potentials. B) The critical concentration is 0.1 M, in which no obvious ion rectification could be observed. C) In high ionic concentration of 1 and 2.5 M, the rectification direction is totally inverted, that is the magnitudes of the currents at positive potentials are higher than those at negative potentials, and cations are preferentially transported from the PPy side to the SPEEK side, which is just opposite with the direction in low salinity. D) The rectification ratio value of the nanochannel both shows ≈ 3 –6 at low and high ionic concentration and ≈ 1 at 0.1 M.

chains to the euryhaline environment. The effect of the length and thickness of PPy on the ionic rectification ratio was also discussed in Section 7 and 8, Supporting Information.

2.3. Euryhaline Ion Selectivity of the Membrane

To further understand the switchable ICR behavior in euryhaline environment, we testified the surface charge density and pore size of the membrane, which affect nanofluidic properties according to the Poisson and Nernst–Planck (PNP) equations.^[12,30,31] First, we have done the visual experiments to confirm the selectivity of the membrane in both dilute and hypersaline solutions as shown in Figure 3A. Confocal laser scanning microscopy (CLSM) is used to characterize the ionic selectivity of the membrane. Two oppositely charged fluorescent dyes (Figure S9, Supporting Information) were used to mark the membrane. The fluorescent dye solution is dropped onto the membrane from only one side and after reacting for 5 min, the membrane was rinsed with deionized water for several times to remove the free dye molecules. Then, the penetration of the dyes through the membrane is observed by CLSM from the other side. In 1×10^{-3} M KCl solution, a fluorescence signal was observed from the membrane dyed by

negatively charged fluorescent dye, indicating the PPy carries some holes here. However, a highly strong fluorescence image was obtained from the membrane with positively charged fluorescent dye in 1 M KCl solution, indicating the abundant negative charge existing on the PPy surface in hypersaline solution. As for the SPEEK side, the surface always selects the positive ions no matter in dilute or concentrated solution. This visual data indicates that the polarity and surface charge density of PPy side are self-adaptively adjusted with the salinity change, which determines the selectivity of the membrane.

2.4. Adaption of Surface Charge and Pore Structure to the Varied Ionic Concentration

The results above demonstrate the performance of PPy side fluctuated with the changing salinity and mainly contribute to the reversal of the ICR direction. To further prove the adaptive change of its surface charge, the zeta potential of PPy sample immersed in a wide range of ionic concentrations is tested as shown in Figure 3B. Before the measurement, the samples are dipped in different concentrations of KCl solutions for 5 min and the testing pH condition is around 5.6. Exposed to the dilute and concentrated KCl solution, the value of zeta

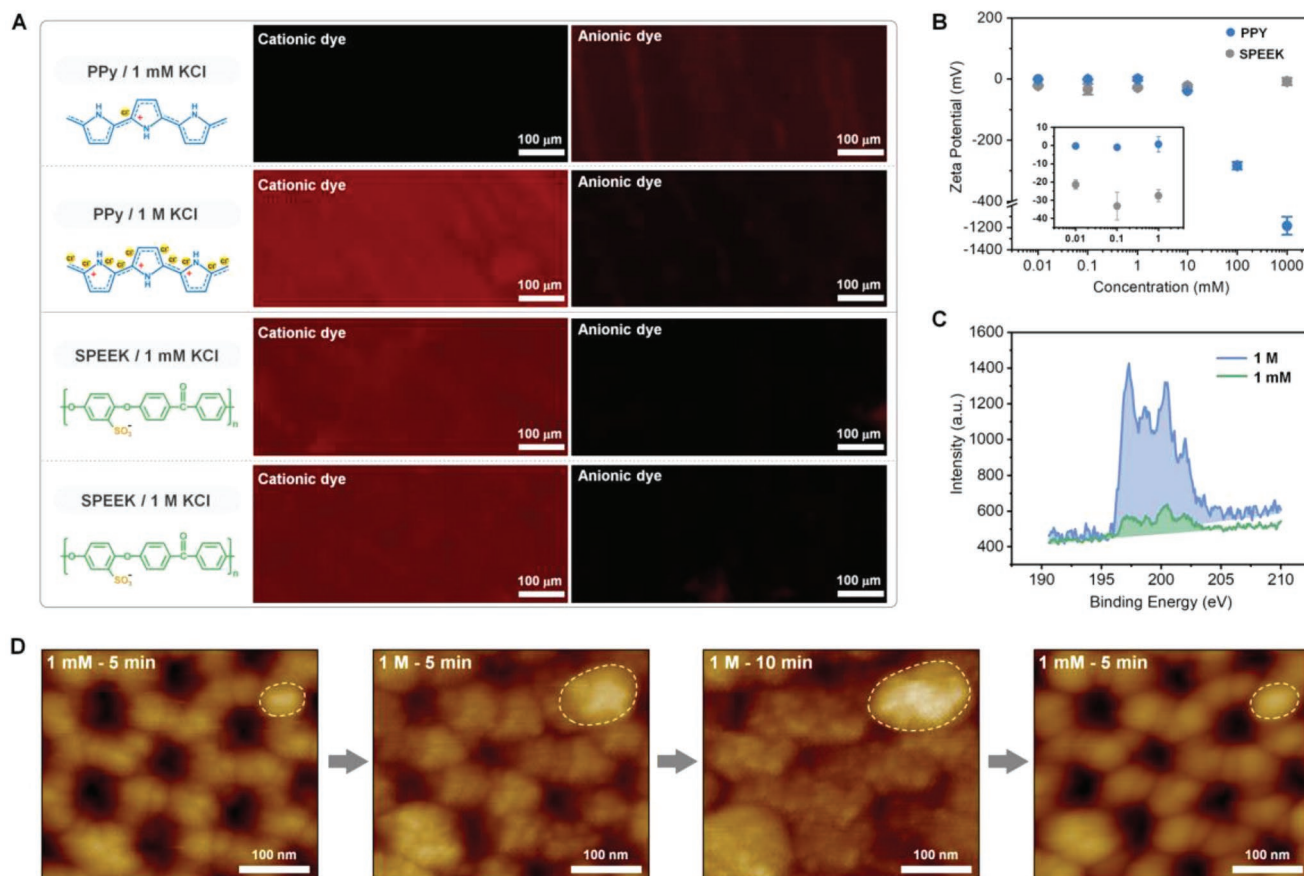


Figure 3. Surface chemistry and physical morphology switch of PPy side induced by salinity change. A) The fluorescence images of the membrane dyed by positively charged fluorescent dye (left) and negatively charged fluorescent dye (right). The negative dye molecule could pass through the PPy dipped in 1×10^{-3} M KCl, while the positive dye molecule could pass through the PPy dipped in 1 M KCl and the SPEEK in 1×10^{-3} M and 1 M KCl. B) Zeta potential of PPy and SPEEK in different concentrations of KCl solutions. Inset: enlarged image of zeta potential in dilute solution (0.01, 0.1, 1×10^{-3} M). The value of SPEEK keeps constant at all concentrations. As for PPy, a dramatic change in the value occurred at 100 mM. C) XPS analysis of PPy side in low and high concentrations of KCl. The intensity and integral area of the chlorine peak treated with 1 M KCl solution are much higher than those of sample treated with 1×10^{-3} M solution. D) In situ AFM images of PPy side immersed in KCl solutions. In 1×10^{-3} M KCl, the polymer is in contracted state. While in 1 M KCl, the polymer chain swells gradually and blocks the pores in hypersaline 10 min later. When the solution was changed back to 1×10^{-3} M KCl, the polymer contracts back again. White circles marked on the images indicate the volume expansion in situ.

potential changed drastically. In the low concentration (0.01 and 0.1×10^{-3} M KCl), the zeta potential is close to 0 mV. However, the value dropped to minus with the concentration rising to 10×10^{-3} M, indicating that the surface charge of PPy sample turns negative in concentrated solutions. A dramatic decline of the zeta potential occurred at 100 mM and when the sample was dipped in high salinity of 1 M solution, the absolute value of the zeta potential reached $\approx 10^3$ times of the dilute solution. Whereas, the zeta potential value of SPEEK samples has no obvious change in a wide salinity range.

Such a big change in charge density allows us to hypothesize that the ions move out from the polymer chain or migrate into it under different osmotic pressure, leading to the different doping degrees of the PPy, which can be demonstrated by the X-ray photoelectron spectroscopy (XPS) data (Figure 3C). For the sample treated by high salinity of 1 M KCl solution, the intensity and integral area of the chlorine peak (Cl2p 197.4, 198.5, 200.8 eV)^[32] are much higher than those of sample treated by low salinity (1×10^{-3} M), proving that chloride ions

from the concentrated solution penetrate into the polymer triggered by the high osmotic pressure and dope with the chain. Besides, the potassium peak (K2p 295 eV)^[33] neither appeared in the XPS spectra of 1×10^{-3} M nor in 1 M KCl treated samples (Figure S10, Supporting Information), suggesting that potassium ions did not migrate into the polymer chains. The influence of ionic strength on the polymer chain doping state is also confirmed by cyclic voltammetry characterization (Section 11, Supporting information).

Recently, scientists have found that doping levels could be tuned by different doping processes.^[27] We hypothesize that the doping chlorine ions move out or penetrate into the PPy brush driven by the osmotic pressure, when immersed in different salinity solutions. Particularly, enormous chlorine ions move into the PPy brush to dope with the monomer unit in concentrated solution. Thus, the retained chlorine ions between the PPy brushes endow the membrane with abundant negative charges, in accord with the zeta potential value. In situ Raman measurements of PPy film at different concentrations

of KCl solutions also prove that enormous ions penetrate into the polymer chains under high osmotic pressure (Section 12, Supporting Information).

Similar to the classic redox doping process,^[34] we also observe the physical morphology switch induced by the ionic concentration directly at nanoscale by in situ atomic force microscopy (AFM) (Figure 3D). Clearly, the polymer chain tends to be more tense and rigid in dilute electrolyte. In this state, the original AAO nanochannel is still open to the external environment with a pore size of ≈ 45 nm. While in hypersaline environment, owing to the massive immigration of doping ions into the polymer, the polymer chain swells, leading to a decrease in pore diameter. It should be noted that, with the dipping time increasing, further expanding of the polymer can be observed, indicating the gradual adaption process of PPy to the hypersaline environment. Apparently, when the expansion process reached a stable level, PPy brushes apparently almost completely block the pores. However, when applied with a voltage, still a large number of ions travel across the membrane, which is demonstrated by the high transmembrane ion current ($857 \mu\text{A}$ in 2.5 M) shown in Figure 2C. Therefore, we hypothesize the PPy chains expand and interpenetrate each other into 3D networked pores to allow the ions to pass through.

As shown in the AFM images, the area of the polymer brush was expanded to ≈ 4.63 times after swelling, and by calculation, the volume was expanded to about ten times. Thus, the local volume fraction of PPy is about $\phi \approx 0.1$, which exceeds the critical overlap concentration ϕ^* ($\approx 10^{-3}$ to 10^{-2}) and is much lower than 1 ($\phi^* < \phi \ll 1$). Therefore, the PPy chains in hypersaline solution could be considered as semidilute condition. In this case, the chains interpenetrate with each other and each monomer is surrounded by solvent, resulting in a 3D networked structure composed of densely packed solvent accessible void spaces. These void spaces between the polymer chains are filled with water, providing ion transport pathways. The average distance between the two overlap points of the chains (the correlation length ξ), can be equivalent to the average pore diameter of the 3D network pores. According to de Gennes' scaling argument, the equivalent pore diameter (the correlation length ξ) could be calculated as^[35]

$$\xi \approx b\phi^{\frac{-\nu}{3\nu-1}} \quad (1)$$

where b is the repeating unit size (≈ 0.34 nm) of PPy, which is calculated by Materials Studio software; ϕ is the volume fraction of PPy (0.1); $\nu \approx 0.588$ is the scaling exponent under good solvent condition. So, the pore size (correlation length ξ) is 1.9 nm. In addition, the pore density can be further estimated as

$$\rho \propto \frac{\left(\frac{D}{\xi}\right)^2}{\pi R^2} \quad (2)$$

where D refers to the average pore diameter of AAO nanochannels (≈ 100 nm) and R is the radius. Thus, the pore density of the 3D network pores is $\approx 10^{13} \text{ cm}^{-2}$. Therefore, when the membrane is shifted from low salinity to hypersaline solution, the original single straight channel (45.0 nm) of PPy side is converted into 3D network porous structures with smaller pore size (1.9 nm) and high pore density ($\approx 10^{13}$). In addition, when

the solution was changed back to a low concentration of 0.001 M KCl, the PPy shrank again and the pore morphology recovered as the straight channel, which demonstrated the reversibility of this salt-induced process (Figure 3D). In conclusion, the charge polarity inverse and pore structure change adaptive to external changing salinity lead to the reversal of the dominant direction of ion transport (Figure S13, Supporting Information).

To our best acknowledge, the adaptive mobile charge with the salinity is never noticed before. It is well-known that high salinity usually negates the effects of selective membranes. However, in this work, the hyper salinity rendered the membrane a large amount of surface charge and enriched the function of the membranes.

2.5. COMSOL Simulation on the Direction-Reversible ICR Phenomena Induced by Ionic Concentration

The salt-induced inversed ICR behavior was also evidenced by the theoretical simulation based on PNP equations. In dilute solutions, the PPy side was modeled as one straight channel and the surface charge density of this side was set as $+0.002 \text{ C m}^{-2}$ (0.001 M KCl) and $+0.001 \text{ C m}^{-2}$ (0.01 M KCl), which were set according to reported works^[16] and estimated by zeta potential value (Section 14, Supporting Information). In concentrated solution, because the PPy side turns into 3D networked pores and to simplify the calculation, this side is modeled as 1D multichannels with smaller pore size (Figure S14, Supporting Information) and the charge density is set as -0.1 C m^{-2} . Other modeling details are provided in Section 15, Supporting Information. Figure 4 shows the simulation results. In dilute solution (1 and $10 \times 10^{-3} \text{ M}$ KCl), the ions in the channel accumulated when applied with a negative bias (-2 V), leading to a high concentration profile. While shifting the direction of the electric field, it formed a depletion zone resulting a low concentration profile (Figure 4A,B). With increasing ionic concentration (1 M), because the polarity of surface charge on the PPy side switches into negativity with higher density and the pore structure turns into multichannels with smaller pore size, the ions are enriched at positive voltage and depleted at negative voltage, which is just opposite to the ion distribution profile at low electrolyte concentration (Figure 4D). At the critical concentration, there is no obvious difference in the ion distribution between the negative bias (-2 V) and positive bias ($+2 \text{ V}$) (Figure 4C). These simulation results are consistent with our experimental data. In this three-section nanochannel, the main performance of one side keeps stable, while the other side is able to adaptively alter its surface charge and pore structure dynamically with the changing ion concentrations, which is the foundation of the reversible rectification behavior in different salinities.

2.6. Salt Endurance and Application

AFM results revealed the gradual adaption process of PPy to the hypersaline environment, which may endow the membrane with excellent salt durability. Therefore, we investigate the salt endurance of ion transport performance of the

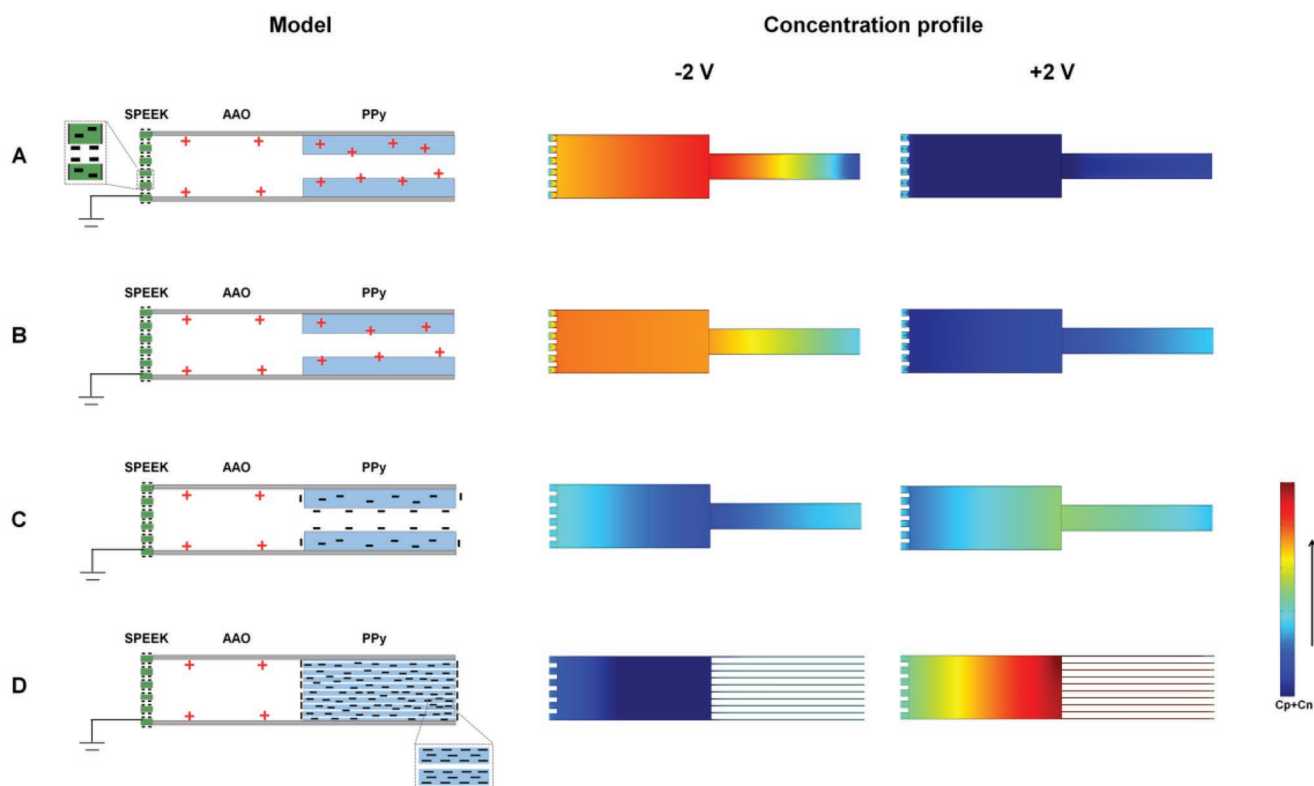


Figure 4. Theoretical simulation of the salt-induced inverted ICR behavior based on PNP equations. A,B) When the ion concentration was $1, 10 \times 10^{-3}$ M and the SPEEK segment is negatively charged and PPy segment is positively charged, the ions in the channel accumulated at negative bias (-2 V) and depleted at positive bias ($+2$ V). C) When the concentration is 0.1 M, there is no remarkable difference in the ion distribution between the negative bias (-2 V) and positive bias ($+2$ V). D) When the concentration increased to 1 M, owing to the polarity of surface charge on the PPy segment switches into negativity with higher density and the pore structure turns into multichannels with smaller pore size, the ions were enriched at positive voltage ($+2$ V) while depleted at negative voltage (-2 V), which is opposite to the ion distribution situation at low electrolyte concentration.

sandwich-structured membrane by testing the variation of transmembrane ion current with dipping time. Compared with the constant ion current of membrane tested in dilute solution (Figure 5A), under high salinity of 1 M KCl, the ion current at positive bias gradually increases with time growth while the negative current keeps stable, attributed to the increasing negative surface charge density of PPy side (Figure 5B). As a result, the calculated ion rectification under high salinity shows a continuous increase and stabilizes at around 30 cycles (42 s for one testing cycle) (Figure 5B). In short, after a period of dynamic interaction between polymer chains and salt solution, the positive ionic current has increased by 900% and the rectification ratio has increased by 45%. Furthermore, when the test environment is switched between 1×10^{-3} M and 1 M for many runs, the membrane performance shows good switchability and stability (Figure 5C).

Salt endurance is a long-standing challenge issue for nanofluidic devices, which is crucial for most water nexus technologies. For example, the power density of osmotic power generator based on nanoporous membranes is limited by charge shielding effect caused by ion enrichment on the membrane surface, which weakens the surface potential and degrades the power generation performance.^[36–38] In our membrane system, the surface of PPy side could be adjusted adaptively with external ion concentrations, the increased charge could weaken

the shielding effect by ion enrichment and the reduction of pore size could shorten the distance between electric double layers, thus leading to the increased selectivity of the membrane. This excellent salt durability and stability of PPy make it potential salinity gradient energy harvester as well. Thus, the PPy-based membrane was constructed to harvest the blue energy. It was fixed between different concentrations of solutions and the collected power could be transferred to external circuit and supply an electronic load (Figure 5D, inset). The high-salinity solution was placed on the PPy side with 5 M NaCl, and the low-salinity solution was 0.01 M and the effective testing membrane area for ion conduction was $\approx 3 \times 10^4 \mu\text{m}^2$. Quite different from the reported power generators before, the power generating current continues to rise up with time growth, increasing by nearly two orders of magnitude and reaches a stable level after ≈ 6 h (Figure 5D), indicating the dynamic adaption process of PPy to the hypersaline environment and the good salt endurance of the membrane. After immersing in salt solution for 12 h until the membrane reached steady state, the salinity gradient power density was then measured. The power density of the resistor in the circuit is calculated using the equation $P_L = I_{\text{osmosis}}^2 R_L$. As shown in Figure 5E, with the increasing load resistance, the current density is reduced and the output power reaches a maximum of 26.22 W m^{-2} at the resistance of $1.8 \text{ k}\Omega$, higher than those of existing nanofluidic systems.^[19,21,39–53] It is noticed

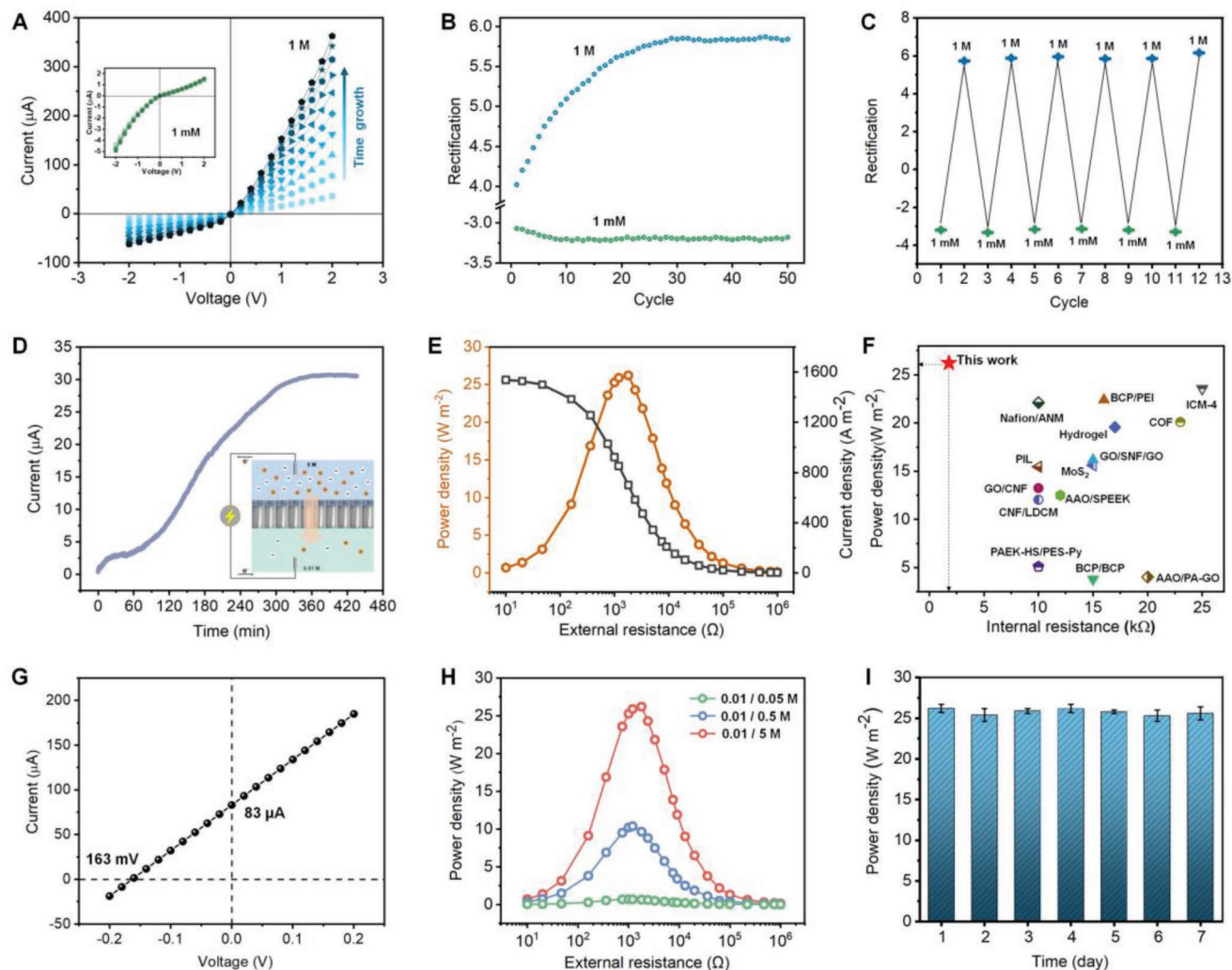


Figure 5. Dynamic self-adaptation of membrane to hypersalinity and its application in osmotic power harvesting. A) Gradual incrementation of the transmembrane ionic current at positive bias of the sandwich-structured membrane in high salinity (1 M KCl) and constant ionic current of the membrane in low salinity (1×10^{-3} M KCl). A 900% incrementation of current in 1 M was obtained before reaching stable. B) Continuously increasing rectification ratio under high salinity and reaching stable at ≈ 30 cycles with a 45% incrementation, while the rectification value in 1 mM keeps nearly constant. C) Pronounced switchability of the membrane performance when shifted between low salinity (1×10^{-3} M KCl) and high salinity (1 M KCl). D) The power generating current keeps rising up with time growth, increasing by nearly two orders of magnitude and reaches a stable level after ≈ 6 h. The inset shows the schematic illustration of the blue energy-harvesting device. The PPy side faces the hypersaline water (5 M NaCl), while another side faces the dilute solution (0.01 M NaCl). The collected power can be output to an external circuit. E) The power generation on the external load under concentration gradient. The current density is reduced with increasing load resistance, while the output power density achieves a maximum value of 26.22 W m^{-2} at the resistance of 1.8 k Ω . F) Comparison with reported membranes to show the superior performance. G) Current–voltage curve of the membrane under a salinity gradient (0.01 M/0.5 M NaCl). H) The power density of the membrane under different salinity gradients. I) The long-term stability of the energy conversion at 500-fold salinity gradient.

that, to our best knowledge, the internal resistance of the membrane (1.8 k Ω) reaches the smallest value among the previously reported osmotic power generators, might for the effective concentration difference between the inlet and outlet of the nanochannels can be maintained owing to the salinity-adaptive properties of the membrane. The comparison with previously reported membranes is shown in Figure 5F.^[19,21,39,40,42,43,46–53]

The current–voltage curve of the membrane at 0.01 M/0.5 M gradient is shown in Figure 5G, in which the open-circuit voltage (V_{open}) of the membrane is ≈ 163 mV, and the diffusion current reaches 83 μA . Thus, the cation transference number

(t_n) can be calculated as ≈ 0.957 , indicating the excellent cation selectivity, which also benefits the high energy-conversion efficiency (η) $\approx 41.9\%$ (Section 16 and Table S1, Supporting Information). In addition, compared with the high ion selectivity under high salinity, values of t_n and η for other salinity gradients in dilute solution were smaller (Table S1, Supporting Information), suggesting the enhanced selectivity of the membrane under a high-salinity environment. Power generation performance under different salinity gradients (fivefold, 50-fold, 500-fold) was also investigated. The low concentration side is fixed at 0.01 M and the high-concentration side is increased

from 0.05 to 5 m. With increasing salinity gradient, the initial current density increases from 305 to 1537 A m⁻² (Figure S15, Supporting Information) and the corresponding output power density reaches its peak value of 0.64, 9.65, and 26.22 W m⁻² respectively for fivefold, 50-fold, and 500-fold salinity gradient (Figure 5H). The salinity gradient energy conversions were also measured under different types of electrolytes at 500-fold salinity gradient (0.01/5 m for LiCl, NaCl, 0.007/3.4 m for KCl). As shown in Figure S16, Supporting Information, the maximum power density was 8.3, 26.22, and 34.1 W m⁻² for LiCl, NaCl, and KCl, respectively. The better performance in KCl solution is owing to the highest diffusion coefficient of K⁺. Moreover, the membrane can work in a wide pH range (Figure S17, Supporting Information) and shows good long-term working stability (Figure 5I). The dependence of power density on the electropolymerization time of PPy, which affects the PPy thickness, was also investigated. Although shortening the thickness can reduce the resistance to increase the power density, lower selectivity caused by short ion pathway will weaken power generation performance. As shown in Figure S18, Supporting Information, the power density reaches a maximum when the polymerization time is in the middle value.

3. Conclusion

Salinity, particularly hypersalinity, is not in favor of nanofluidic science. The classic ionic nanofluidic behavior, like ionic selectivity, ICR, etc., tends to disappear with the increased ionic strength. To address this challenge, scientists have developed nanoporous membrane with narrow pores and abundant surface charges.^[54–56] In general, these design strategies based on fixing a factor could make nanofluidic work in some certain condition. Inspired by euryhaline salmon, we designed a salinity self-adaptive ion diode with a direction-reversed rectification, based on the SPEEK/AAO/PPy structure. Ions inside the channel are transported in the completely opposite direction under low-salt and high-salt conditions. Different osmotic pressures lead to the dynamic interactions between solvent ions and PPy chains. Ion penetration into PPy under high pressure endows the polymer chain with a high surface charge, rendering the membrane-based osmotic power generator with power density up to 26.22 Wm⁻². Different from the previously reported salt-resistant membranes whose polymer performance remains constant in the process of changing the solution, the performance parameters including charge polarity, density, and pore structure of PPy side, are all adaptively altered with the changing concentrations, which leads to the opposite ion transport direction. The special salinity adaptability and good salt endurance enable the membrane to possess high charge density and small pore size under high salinity, overcoming the shielding effect of strong ion strength on the electric double layer for traditional membranes, leading to the improved ion selectivity and power generation performance. High salinity, which has negative influence on power generator, can be turned into a favorable factor in our salinity-adaptive membrane system. At the same time, due to the dynamic balance between the solvent ions and the PPy chains, the reversible diode behavior is durable and repeatable. In addition, PPy

with variable volume is designed to embed and grow inside the nanopores of AAO, which provides a confined space for its directed inward expansion, in favor of observing its adaptive changes in the nanometer scale.

4. Experimental Section

Materials: The AAO nanoporous membranes were purchased from HeFei PuYuan Nano Technology Co., Ltd. Pyrrole (Py), hydrochloric acid (HCl), potassium chloride (KCl), sulfuric acid (H₂SO₄), 1-methyl-2-pyrrolidinone (NMP), sulfonated rhodamine, and propidium iodide were purchased from Sigma Aldrich. High-purity water with a resistivity of 18.2 MΩ cm⁻¹ was produced by a Milli-Q Reference water-purification system. All reagents and solvents were used without further purification unless otherwise noted. Ag/AgCl electrodes were used to apply a transmembrane potential.

Preparation of SPEEK: SPEEK was prepared through the sulfonation reaction between poly(ether ether ketone) (PEEK) and sulfuric acid. PEEK powder (1.4 g) was dissolved in sulfuric acid (10 mL) and then the mixture was heated at 40 °C. Under vigorous stirring, the sulfonation reaction was kept for 10 h. The as-prepared yellow solution was poured into ice water to form white solid product, which was collected and washed with deionized water thoroughly until pH reached 7. The obtained sulfonated product, which was called SPEEK, was then dried at 80 °C in vacuum.

Fabrication of the Sandwich-Structured Membrane: The AAO templates were first cleaned by ultrasonic treatment in 0.1 m HCl solution, deionized water, and ethanol for 1 min, respectively. To carry out the electrochemical polymerization, a conductive Au layer was deposited on the top side of the AAO membrane by ion sputtering. The electrochemical polymerization of PPy was performed in a three-electrode system with the AAO template as the working electrode, a copper sheet as the counter electrode, and a saturated Hg/HgCl₂ electrode as the reference electrode. The electrolyte consists of an aqueous HCl (0.5 m) and pyrrole monomer (0.05 m) solution. The electrochemical deposition was carried out by a cyclic voltammetry method with a low *E* of -0.1 V and a high *E* of 1 V for 280 s. After electropolymerization, the membranes were immersed into ethanol for three times to remove the impurity. The solution of the SPEEK in *N*-methyl pyrrolidone (NMP) (0.14 g mL⁻¹) was spin-coated on the bottom side of the as-prepared membrane and dried at 80 °C in a vacuum oven for 3 h. Thus, the asymmetric membrane with the ionomer/AAO/conducting polymer sandwich-structured nanochannels was obtained.

Calculation of the Critical Overlap Concentration ϕ^* of PPy: The critical overlap concentration ϕ^* of PPy could be calculated as^[57]

$$\phi^* = N^{1-3\nu} \quad (3)$$

where *N* is the number of repeating units (≈100–1000) of PPy,^[58] $\nu \approx 0.588$ is the scaling exponent under good solvent condition. So, the critical overlap concentration ϕ^* is ≈0.005–0.03.

Supporting Information

Supporting Information is available from the Wiley Online Library or from the author.

Acknowledgements

This work was funded by the National Science Foundation of China (grant 21875270, 21988102) and the Youth Innovation Promotion Association of CAS (Grant No. 2021029).

Note: Spelling errors in Section 1 (on page 1 and 2) were corrected on August 4, 2022, after initial publication online.

Conflict of Interest

The authors declare no conflict of interest.

Author Contributions

Y.Z. and L.J. conceived the idea. J.H. performed the experiments. Y.Z. and J.J.Z. analyzed and interpreted the results. J.H. and Y.Z. drafted the manuscript and all authors contributed to the writing of the manuscript.

Data Availability Statement

The data that support the findings of this study are available from the corresponding author upon reasonable request.

Keywords

ion rectification, nanofluidic diodes, salinity-adaptive membranes, salinity-gradient power generation

Received: April 6, 2022

Revised: June 4, 2022

Published online: June 29, 2022

-
- [1] F. H. Epstein, A. I. Katz, *Science* **1967**, 156, 1245.
 [2] J. Teyssier, S. V. Saenko, D. van der Marel, M. C. Milinkovitch, *Nat. Commun.* **2015**, 6, 6368.
 [3] M. Weisbart, *Can. J. Zool.* **1968**, 46, 385.
 [4] S. L. Edwards, W. S. Marshall, *Fish Physiol.* **2012**, 32, 1.
 [5] L. A. Sampaio, A. Bianchini, *J. Exp. Mar. Biol. Ecol.* **2002**, 269, 187.
 [6] D. Kültz, *J. Exp. Biol.* **2015**, 218, 1907.
 [7] C. G. Nichols, A. N. Lopatin, *Annu. Rev. Physiol.* **1997**, 59, 171.
 [8] X. Sui, Z. Zhang, Z. Zhang, Z. Wang, C. Li, H. Yuan, L. Gao, L. Wen, X. Fan, L. Yang, X. Zhang, L. Jiang, *Angew. Chem., Int. Ed.* **2016**, 55, 13056.
 [9] M. Ali, S. Mafe, P. Ramirez, R. Neumann, W. Ensinger, *Langmuir* **2009**, 25, 11993.
 [10] H. Daiguji, Y. Oka, K. Shirono, *Nano Lett.* **2005**, 5, 2274.
 [11] I. Vlasiouk, Z. S. Siwy, *Nano Lett.* **2007**, 7, 552.
 [12] R. Yan, W. Liang, R. Fan, P. Yang, *Nano Lett.* **2009**, 9, 3820.
 [13] C. B. Picallo, S. Gravelle, L. Joly, E. Charlaix, L. Bocquet, *Phys. Rev. Lett.* **2013**, 111, 244501.
 [14] G. Pérez-Mitta, W. A. Marmisollé, C. Trautmann, M. E. Toimil-Molares, O. Azzaroni, *J. Am. Chem. Soc.* **2015**, 137, 15382.
 [15] H. S. White, A. Bund, *Langmuir* **2008**, 24, 2212.
 [16] B. Bao, J. Hao, X. Bian, X. Zhu, K. Xiao, J. Liao, J. Zhou, Y. Zhou, L. Jiang, *Adv. Mater.* **2017**, 29, 1702926.
 [17] I. Vlasiouk, S. Smirnov, Z. Siwy, *ACS Nano* **2008**, 2, 1589.
 [18] Y. Zhou, L. Jiang, *Joule* **2020**, 4, 2244.
 [19] X. Zhu, J. Hao, B. Bao, Y. Zhou, H. Zhang, J. Pang, Z. Jiang, L. Jiang, *Sci. Adv.* **2018**, 4, eaau1665.
 [20] G. Laucirica, M. E. Toimil-Molares, C. Trautmann, W. Marmisollé, O. Azzaroni, *ACS Appl. Mater. Interfaces* **2020**, 12, 28148.
 [21] C. Li, L. Wen, X. Sui, Y. Cheng, L. Gao, L. Jiang, *Sci. Adv.* **2021**, 7, eabg2183.
 [22] S. Kim, Y. Wang, J. Lee, H. Jang, J. Han, *Phys. Rev. Lett.* **2007**, 99, 044501.
 [23] J. Xiao, H. Zhan, X. Wang, Z. Xu, Z. Xiong, K. Zhang, G. P. Simon, H. Zhan, X. Wang, Z. Xu, J. Z. Liu, D. Li, *Nat. Nanotechnol.* **2020**, 15, 683.
 [24] X. Yang, C. Cheng, Y. Wang, L. Qiu, D. Li, *Science* **2013**, 341, 534.
 [25] R. Giridharagopal, L. Q. Flagg, J. S. Harrison, M. E. Ziffer, J. Onorato, C. K. Luscombe, D. S. Ginger, *Nat. Mater.* **2017**, 16, 737.
 [26] C. Y. Lin, E. T. Acar, J. W. Polster, K. Lin, J. P. Hsu, Z. S. Siwy, *ACS Nano* **2019**, 13, 9868.
 [27] Y. Yamashita, J. Tsurum, M. Ohno, R. Fujimoto, S. Kumagai, T. Kurosawa, T. Okamoto, J. Takeya, S. Watanabe, *Nature* **2019**, 572, 634.
 [28] I. E. Jacobs, Y. Lin, Y. Huang, X. Ren, D. Simatos, C. Chen, D. Tjhe, M. Statz, L. Lai, P. A. Finn, W. G. Neal, G. D'Avino, V. Lemaur, S. Fratini, D. Beljonne, J. Strzalka, C. B. Nielsen, S. Barlow, S. R. Marder, I. McCulloch, H. Sirringhaus, *Adv. Mater.* **2021**, 34, 2102988.
 [29] Asano, N. M. Aoki, S. Suzuki, K. Miyatake, H. Uchida, M. Watanabe, *J. Am. Chem. Soc.* **2006**, 128, 1762.
 [30] Bocquet, L., *Nat. Mater.* **2020**, 19, 254.
 [31] D. Stein, M. Kruithof, C. Dekker, *Phys. Rev. Lett.* **2004**, 93, 035901.
 [32] J. Tabačiarová, M. Mičušík, P. Fedorko, M. Omastová, *Polym. Degrad. Stab.* **2015**, 120, 392.
 [33] S. Li, E. T. Kanga, K. G. Neoha, Z. H. Ma, K. L. Tan, W. Huang, *Appl. Surf. Sci.* **2001**, 181, 201.
 [34] M. Brinker, G. Dittrich, C. Richert, P. Lakner, T. Krekeler, T. F. Keller, N. Huber, P. Huber, *Sci. Adv.* **2020**, 6, eaba1483.
 [35] M. Rubinstein, R. H. Colby, *Polymer Physics*, Oxford University Press, Oxford, UK **2003**.
 [36] J. Gao, W. Guo, D. Feng, H. Wang, D. Zhao, L. Jiang, *J. Am. Chem. Soc.* **2014**, 136, 12265.
 [37] Z. Zhang, L. He, C. Zhu, Y. Qian, L. Wen, L. Jiang, *Nat. Commun.* **2020**, 11, 875.
 [38] K. Xiao, L. Jiang, M. Antonietti, *Joule* **2019**, 3, 2364.
 [39] W. Chen, T. Dong, Y. Xiang, Y. Qian, X. Zhao, W. Xin, X. Kong, L. Jiang, L. Wen, *Adv. Mater.* **2022**, 34, 2108410.
 [40] Y. Hu, Y. Teng, Y. Sun, P. Liu, L. Fu, L. Yang, X. Kong, Q. Zhao, L. Jiang, L. Wen, *Nano Energy* **2022**, 97, 107170.
 [41] S. Hong, J. K. El-Demellawi, Y. Lei, Z. Liu, F. A. Marzooqi, H. A. Arafat, H. N. Alshareef, *ACS Nano* **2022**, 16, 792.
 [42] C. Chang, C. Chu, Y. Su, L. Yeh, *J. Mater. Chem. A* **2022**, 10, 2867.
 [43] Q. Luo, P. Liu, L. Fu, Y. Hu, L. Yang, W. Wu, X. Kong, L. Jiang, L. Wen, *ACS Appl. Mater. Interfaces* **2022**, 14, 13223.
 [44] P. Luan, Y. Zhao, Q. Li, D. Cao, Y. Wang, X. Sun, C. Liu, H. Zhu, *Small* **2021**, 18, 2104320.
 [45] X. Zhao, C. Lu, L. Yang, W. Chen, W. Xin, X. Kong, Q. Fu, L. Wen, G. Qiao, L. Jiang, *Nano Energy* **2021**, 81, 105657.
 [46] Z. Zhang, X. Sui, P. Li, G. Xie, X. Kong, K. Xiao, L. Gao, L. Wen, L. Jiang, *J. Am. Chem. Soc.* **2017**, 139, 8905.
 [47] W. Chen, Q. Wang, J. Chen, Q. Zhang, X. Zhao, Y. Qian, C. Zhu, L. Yang, Y. Zhao, X. Kong, B. Lu, L. Jiang, L. Wen, *Nano Lett.* **2020**, 20, 5705.
 [48] S. Hou, W. Ji, J. Chen, Y. Teng, L. Wen, L. Jiang, *Angew. Chem., Int. Ed.* **2021**, 60, 9925.
 [49] C. Zhu, P. Liu, B. Niu, Y. Liu, W. Xin, W. Chen, X. Kong, Z. Zhang, L. Jiang, L. Wen, *J. Am. Chem. Soc.* **2021**, 143, 1932.
 [50] W. Xin, H. Xiao, X. Kong, J. Chen, L. Yang, B. Niu, Y. Qian, Y. Teng, L. Jiang, L. Wen, *ACS Nano* **2020**, 14, 9701.
 [51] L. Zhang, S. Zhou, L. Xie, L. Wen, J. Tang, K. Liang, X. Kong, J. Zeng, R. Zhang, J. Liu, B. Qiu, L. Jiang, B. Kong, *Small* **2021**, 17, 2100141.
 [52] Y. Wu, W. Xin, X. Kong, J. Chen, Y. Qian, Y. Sun, X. Zhao, W. Chen, L. Jiang, L. Wen, *Mater. Horiz.* **2020**, 7, 2702.
 [53] S. Hou, Q. Zhang, Z. Zhang, X. Kong, B. Lu, L. Wen, L. Jiang, *Nano Energy* **2021**, 79, 105509.

- [54] R. H. T unugntla, F. I. Allen, K. Kim, A. Belliveau, A. Noy, *Science* **2017**, 357, 792.
- [55] J. Lu, H. Zhang, J. Hou, X. Li, X. Hu, Y. Hu, C. D. Easton, Q. Li, C. Sun, A. W. Thornton, M. R. Hill, X. Zhang, G. Jiang, J. Z. Liu, A. J. Hill, B. D. Freeman, Lei Jiang, H. Wang, *Nat. Mater.* **2020**, 19, 767.
- [56] A. Siria, P. Poncharal, A. L. Bianco, R. Fulcrand, X. Blase, S. T. Purcell, L. Bocquet, *Nature* **2013**, 494, 455.
- [57] P. G. de Gennes, *Scaling Concepts in Polymer Physics*, Cornell University, Ithaca, NY, USA **1980**.
- [58] G. B. Street, S. E. Lindsey, A. I. Nazzal, K. J. Wynne, *Mol. Cryst. Liq. Cryst.* **1985**, 118, 137.